Contents

1 Introduction **1**

1.1 Free-standing nanowires 1

1.2 Experimental growth techniques 2

1.3 Practical applications 4

1.4 Motivation of this thesis work 5

1.5 Organization of this thesis 6

2 Cylindrical nanowire **9**

2.1 Analytical solution 9

2.2 Numerical solution 11

3 Cylindrical nanowire with bulge **15**

3.1 A numerical study of a bulged wire 15

3.2 A discussion on the parameter $\langle z^2 \rangle$ 18

3.3 A comparison with a 2D model 24

4 Cylindrical wire with magnetic field **27**

4.1 Analytical calculations for the infinitely long cylindrical wire 27

4.2 Numerical calculations for the infinitely long cylindrical wire 29

4.3 Numerical solution for a finite cylindrical wire 30

4.4 Numerical solution for a bulged wire 31

5 Conclusion 37

References 39

1

Introduction

In recent years we have witnessed the emerging of a rapidly breeding area of extensive and intellectually challenging research on nanoscale structures across many fronts of both physical sciences and engineering. Nanostructures, by definition, are systems of which at least one dimension is within nanometer scale, that is, reducing 1, 2 or 3 dimensions of a bulk material to the nanometer scale produces nanometer thick two-dimensional (2D) layers, one-dimensional (1D) nanowires, or zero-dimensional (0D) nanoclusters, respectively. Two interesting questions emerge: (i) how can nanostructures of specific nanoscale dimension(s) be synthesized or fabricated in a systematical manner, and (ii) what are the associated intrinsic and possibly unique physical properties of thus produced nanostructures? In this introduction, we focus on these questions in the context of 1D nanostructures: nanowires.

1.1 FREE-STANDING NANOWIRES

One class of nanowires are the free-standing nanowires (see Fig. 1.1). Experimentally they are observed to have aspect ratios (the ratio between length to width) of 1000 or more. As such they are often referred to as $1-$dimensional materials. For example, silicon (Si) nanowires have diameters of $20 \sim 50$ nm, and can be hundreds of micrometers long[1]. Other important examples are based on semiconductors such as InP, GaN, etc., dielectrics (e.g. SiO_2,TiO_2), or metals (e.g. Ni, Pt), with typical diameters from a few nanometers to sev-

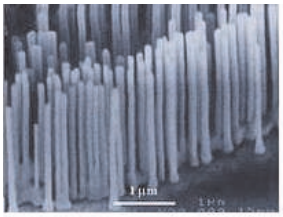

Fig. 1.1 The arrays of free-standing nanowire under an electron microscope. Photo by Peidong Yang/UC Berkeley[2].

eral hundred nanometers.
Nanowires have many interesting properties that are not seen in bulk or three-dimensional (3D) materials. This is because electrons in nanowires are quantum confined laterally and thus occupy energy levels that are different from the traditional continuum of energy levels or bands found in bulk materials. Peculiar features of this quantum confinement exhibited by certain nanowires such as carbon nanotubes manifest themselves in discrete values of the electrical conductance. Such discrete values arise from a quantum mechanical restraint on the number of electrons that can travel through the wire at the nanometer scale.

1.2 EXPERIMENTAL GROWTH TECHNIQUES

Our focus on nanoscale wires is motivated by basic scientific and technology questions. Nowadays there are still not fairly well-developed methods that address the question as to how atoms or other building units can be arranged into wirelike structures, that is, structures with nanoscale diameter and much longer bulk length, as opposed to the synthesis of 0D nanoclusters via arrested precipitation and the growth of 2D layers using molecular beam epitaxy (MBE). Researchers have adopted several strategies to synthesize wirelike nanostructures. For example, chemical vapor deposition (CVD) or MBE on the surfaces activated by a growth catalyst is used to grow semiconductor nanowires. In addition, template directed synthesis has been used to prepare 1D nanostructures[3]. Although a promising and relatively simple technique, template directed growth generally produces polycrystalline materials with diameters greater than 10 nm, which limits its application scope. Alternative growth techniques may also include magnetron sputtering deposition (MSD), which may answer the economical and ecological call of nanowire production, as well as that of a reasonably high production rate and better wire aspect ratio. The main approach that yields single crystal wirelike structures is vapor-liquid-solid (VLS) growth. It was discovered in 1964

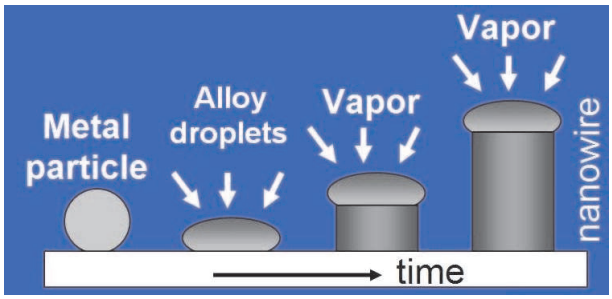

Fig. 1.2 Basic process for VLS growth.

by Wagner and others[4], and later Givargizov developed the first theoretical model to describe the growth process[5]. In the beginning of 1990s, Hiruma *et al*[6] start to grow semiconductor whiskers at nanometer dimensions via CVD. Since late 1990s, C. M. Lieber et al[7][8][9] have investigated the doped nanowire for electronics, photonics and biosensor applications. The basic process of VLS method can be demonstrated as in Fig. 1.2. In VLS growth, a liquid metal cluster or catalyst acts as the energetically favored site for vapor-phase reactant adsorption and the nucleation site for crystallization when supersaturated. Preferential 1D growth occurs in the presence of reactant as long as the catalyst remains liquid. Most previous 1D structures produced by VLS growth have had diameters $\geq 1\mu$m. This relatively large lower size limit is determined by large by the minimum diameter liquid metal catalyst that is achievable under the equilibrium conditions typically used for growth. Recently C. M. Lieber[10] has adopted laser ablation of the catalyst material to achieve nanowire growth (See Fig. 1.3.where the laser-ablation method proposed by C. M. Lieber is demonstrated), with production of nanowire of diameter on the order of 10 nm, or even smaller.

This technique chooses as source material either a feed gas or laser ablated particles. The source, exposed to a catalyst which often comes in the form of liquid metal (such as gold) nanoclusters, then enters these nanoclusters and begins to saturate it. Once supersaturation is reached, the source solidifies and grows outward from the nanocluster. The final product's length can be adjusted by simply turning off the source. Compound nanowires with super-lattices of alternating elements can be produced by switching between different sources while still in the growth phase (see Fig. 1.4 for a demonstration of an InAs/InP superlattice wire).

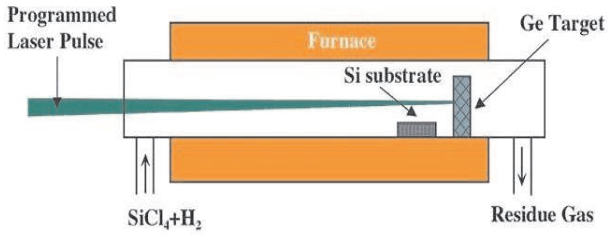

Fig. 1.3 Alternative process using laser ablation for VLS growth. The output from a pulsed laser is focused onto a target located within a quartz tube[10].

1.3 PRACTICAL APPLICATIONS

In terms of practical applications, 1D structures with nanometer diameters, such as nanowires and nanotubes, have great potential for testing and understanding fundamental concepts about the roles of dimensionality and size on physical properties. As stated before, 1D systems should exhibit density of states singularities, can have energetically discrete molecular states extending over large linear distances and may show more exotic phenomena, such as spin-charge separation predicted for a Luttinger liquid[12]. There are also many applications where 1D nanostructures could be exploited, including (i) nanoelectronics, (ii) functional, nanostructure materials, (iii) novel probe microscopy tips and (iv)other 1D nanostructured materials. To realize these and other exciting uses of 1D nanostructures will, however, require an understanding of the fundamental chemistry and physics questions raised above.
(i) Nanoelectronics: Since nanowires and nanotubes carry charge and excitons easily, they are potentially ideal building blocks, with regards to nanoscale electronics and optoelectronics, transport devices such as resonant tunnelling, single-electron transistors, and optoelectronic devices such as optically active quantum dots inside nanowire, e.g. see Fig. 1.5 for Photoluminescence spectra from a single GaInAs Quantum Dot positioned inside a GaAs nanowire from [11]
(ii) Functional, nanostructure materials: Boron-doped silicon nanowires for highly sensitive, real-time electrically based sensors for biological and chemical species (see Fig. 1.6 from [9] for a demonstration of a nanowire nanosensor for pH detection).
(iii) Novel mechanic structure: In [10], C. M. Lieber investigated the possibility of exploiting the remarkable mechanical properties of nanowire and nanotubes in mechanical applications, such as probes for AFM. (See Fig. 1.7)
(iv) Other nanostructured materials: For example, in [10], it is proposed by C. M. Lieber that the incorporation of 1D nanostructure into a high-temperature superconductor (HTS) matrix will result in columnar defects which are beneficial in reducing thermally induced flux motion that limits the critical current

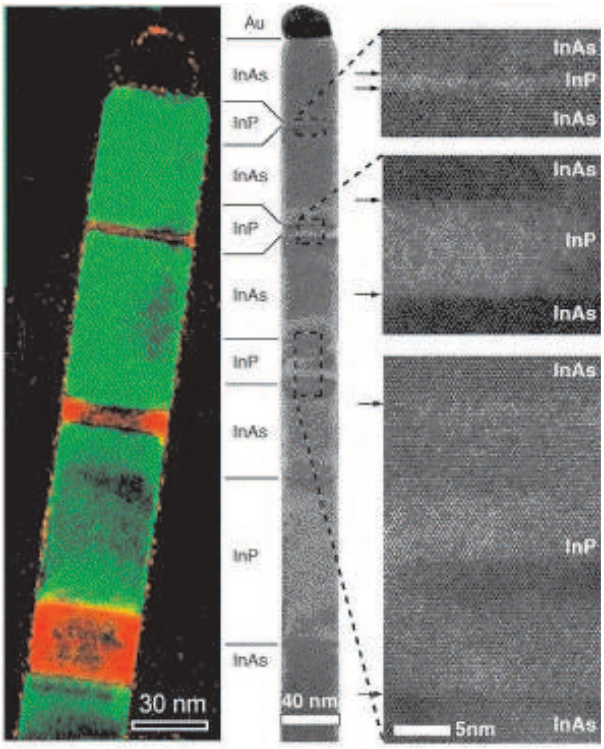

Fig. 1.4 Left-hand figure shows a color-coded representation of the origin of diffraction spots from the two lattices of InAs (green) and InP (red). The right-hand figure shows a high-resolution electron microscope image of the same structure from which one can deduce that the multiple layer structure of alternating InAs and InP segments are perfect from a crystalline point of view, are free of strain within less than 10 nm from the interface, and have an interface abruptness on the atomic level[11].

density (J_c), thereby effecting a large enhancement of J_c in the nanowire/HTS composites.
The development of aforementioned and other functional 1D nanostructured materials promises to be an exciting and challenging area for nanophysics as well as nanoscale chemistry.

1.4 MOTIVATION OF THIS THESIS WORK

As stated before, the intriguing nature and remarkable potentials of the nanowire draw our attention to it, in search for better understanding of the physics underlying these interesting 1D nanostructures. In addition, experimentally grown nanowires are not ideally homogeneous cylindrical structures,

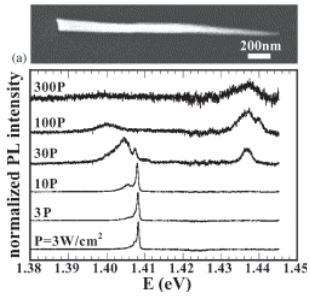

Fig. 1.5 Photoluminescence spectra from a single GaInAs Quantum Dot positioned inside a GaAs nanowire shown as function of the excitation intensity[11].

that is, they exhibit structural heterogeneities, e.g., single or multiple bulges along the length, changing the energy spectrum as well as the electronic transport properties of the nanowire, which is why we address this topic in later chapters. Furthermore, although in normal applications a nanowire is not often found to be exposed to very strong magnetic fields, we nevertheless find that an extra-applied magnetic field to be a very useful tool in probing the intrinsic properties of nanowires, as well as those altered by aforementioned structural heterogeneities. As a result, an extensive investigation of the influence of an applied magnetic field is therefore also included.

1.5 ORGANIZATION OF THIS THESIS

This thesis is divided as follows: Chapter 2 introduces the basic wire model with both analytical and numerical results from simulation, Chapter 3 focuses on the model of a wire with a bulge and Chapter 4 discusses the influence of magnetic field on a cylindrical wire as well as a wire with a bulge.

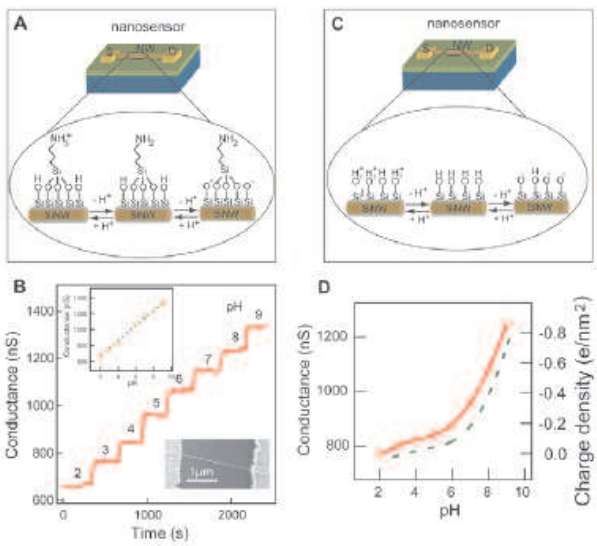

Fig. 1.6 Nanowire pH sensor. (A) Schematic of an amino-functionalized nanowire device and the protonation/deprotonation equilibriums that change the surface charge state with pH. (B) Change in nanowire conductance as the pH of solutions delivered to the sensor is varied from 2 to 9; inset is a plot of conductance data versus pH. (C) Schematic of an unmodified nanowire sensor containing silanol groups and the protonation/deprotonation equilibriums that change the surface charge state with pH. (D) Conductance of an unmodified Si nanowire device (red) versus pH. The dashed green curve is a plot of the surface charge density for silanol groups on silica as a function of pH (Adapted from [9]).

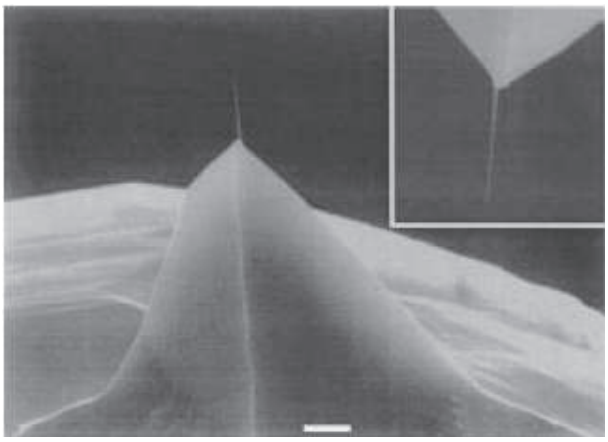

Fig. 1.7 SEM image of a multi-wall nanotube tip attached to a silicon cantilever tip assembly. The inset corresponds to a higher magnification view that highlights the nanotube. The orientation of the inset is rotated 180° relative to the main image. The white bar corresponds to 1 μm. Adapted from [10].

2

Cylindrical nanowire

In this first chapter, we will first give the analytical solution for the single particle wave function and energy spectrum of a cylindrical nanowire. These results will be used later to verify our numerical procedure and serve as a basis for further numerical work, which cannot be done analytically anymore.

2.1 ANALYTICAL SOLUTION

For an ideal quantum wire with infinite length, its Hamiltonian can be written as

$$H = \frac{\vec{p}^{\,2}}{2m} + V\left(x, y, z\right) \tag{2.1}$$

where the potential $V(x, y, z) = V(\vec{r})$ satisfies

$$V(\vec{r}) = \begin{cases} 0 & \rho \leq R \\ \infty & \rho > R, \end{cases}$$

with $\rho = \sqrt{x^2 + y^2}$. It is convenient to use cylindrical coordinates $\vec{r} = (\rho, \theta, z)$ in our system in question, therefore the Schrödinger equation

$$H\psi = E\psi \tag{2.2}$$

becomes

$$\frac{1}{\rho}\frac{\partial}{\partial\rho}\left(\rho\frac{\partial\psi}{\partial\rho}\right)+\frac{1}{\rho^2}\frac{\partial^2\psi}{\partial\theta^2}+\frac{\partial^2\psi}{\partial z^2}+\frac{2m}{\hbar^2}E\psi=0. \tag{2.3}$$

To separate the variables, we assume that ψ can be written as

$$\psi\left(\rho,\theta,z\right)=\varphi\left(\rho,z\right)\phi\left(\theta\right). \tag{2.4}$$

Inserting the above formula into Eq. (2.3), we get

$$0 = \frac{1}{\rho}\frac{\partial}{\partial\rho}\left(\rho\frac{\partial\varphi}{\partial\rho}\right)+\frac{\partial^2\varphi}{\partial z^2}+\frac{2m}{\hbar^2}E\varphi-l^2\varphi \tag{2.5}$$

$$\frac{\partial^2\phi}{\partial\theta^2} = -l^2\theta \tag{2.6}$$

The solution to Eq. (2.6) is given by $\phi=e^{il\theta}$, where l is the angular momentum quantum number.
For Eq. (2.5), we further separate the variables with $\varphi=Ae^{ik_zz}\varrho\left(\rho\right)$, which readily gives

$$\frac{d^2\varrho}{d^2\rho^2}+\frac{1}{\rho}\frac{d\varrho}{d\rho}+\left(\mu^2-\frac{l^2}{\rho^2}\right)\varrho=0 \tag{2.7}$$

where $\mu^2=k^2-k_z^2$, and $k^2=2mE/\hbar^2$. Substituting ρ by x/μ, we then find the solution to Eq. (2.5)

$$\varrho\left(\rho\right)=J_l\left(x\right)=J_l\left(\mu\rho\right)=J_l\left(x_n^{(l)}\frac{\rho}{R}\right) \tag{2.8}$$

where $J_l\left(x\right)$ is Bessel function to the l-th order, $x_n^{(l)}$ is the n-th zero of the Bessel function to the l-th order.
The total wave function can then be written as

$$\psi_{n,l,l_z}=A_{n,l}e^{il\theta}e^{ik_zz}J_l(x_n^{(l)}\frac{\rho}{R}) \tag{2.9}$$

where $A_{n,l}$ is the normalization constant.
Consider boundary condition $\varrho\left(R\right)=0$, we finally attain the energy spectrum as

$$E=\frac{\hbar^2}{2m}\left(\left(\frac{x_n^{(l)}}{R}\right)^2+k_z^2\right). \tag{2.10}$$

Introducing R as the unit of length, and $E_0=\frac{\hbar^2}{2m}$ as the unit of energy, we will obtain the dimensionless energy $\epsilon=((x_n^{(l)})^2+k_z^2R^2)=E/E_0$.

2.2 NUMERICAL SOLUTION

To solve this problem and obtain the above mentioned wave function and the energy spectrum numerically, we make use of COMSOL. This software enables the user to model virtually any 3, 2 or 1 -dimensional problem, and works as follows: an equation can be chosen from an equation library and parameters can be specified as input. Then a geometry has to be defined in which the selected equation has to be solved. COMSOL divides the geometry into finite elements and calculates the solution so that it is known in every point of space.
To obtain numerical results for an infinite wire, we could solve the appropriate equation in a circular geometry, but keeping in mind that, later, we would like to change the wire radius as a function of the length Z/R of the wire. Therefore it is more convenient to introduce the model of the half cross-section through the cylindrical axis, as shown in Fig. 2.1.
The equation that we solve in this 2D system can be obtained from Eq. (2.5). The dimensionless version of Eq. (2.5) is then

$$\frac{1}{\rho'}\frac{\partial}{\partial\rho'}\left(\rho'\frac{\partial\varphi}{\partial\rho'}\right)+\frac{\partial^2\varphi}{\partial z'^2}+\epsilon\varphi-l^2\varphi=0 \tag{2.11}$$

where ρ' and z' denote the dimensionless radius component ρ/R and z-axis component z/R. The dimensionless energy is then $x_n^{(l)2}$, the square of zeros of the Bessel functions.

However, by using this model, it is clear that we also introduce an error: the wire is no longer infinite. Nevertheless, if the height of the wire is considerably larger than the wire radius, the induced error will be significantly lowered.
To determine a proper value of the wire height Z, we will investigate the influence of this value, together with that of the boundary condition (Neumann or Dirichlet) at $z = 0$ and $z = Z$. (The other boundary conditions cannot be chosen and are inherent to the model: $\psi|_{\rho/R=1} = 0$, and $\psi|_{\rho/R=0} = 0$ for $l = 1$ and $\frac{\partial\psi}{\partial\rho}|_{\rho/R=0} = 0$ for $l = 0, 2, 3...$)
In Fig. 2.2 and Fig. 2.3 the deviation of the calculated ground state energy with respect to the analytical value of the energy is shown (on a logarithmic scale) as a function of the wire length Z/R for different boundary conditions and $l = 0, 1$ and 2.

As seen from the figures, Neumann boundary conditions quickly converge to a good approximation, while Dirichlet boundary conditions converge much slower, therefore for computational resources, it is advisable to adopt the Neumann boundary condition. We chose to set the wire length to 25, which is already a good approximation, according to Fig. 2.2.
For practical consideration in the COMSOL environment, we also adopt peri-

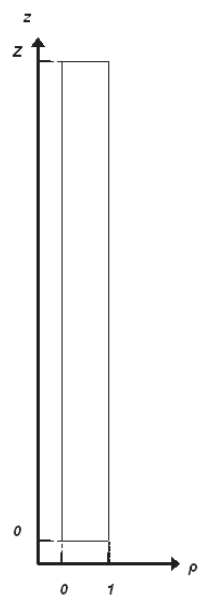

Fig. 2.1 The basic wire model

odic boundary conditions, i.e., we impose that the wave function value and its derivative at $z = 0$ and $z = Z$ are the same, in order to eliminate unphysical solutions.

For such a simple wire model, the result is shown in Fig. 2.4, showing a contour plot of the wave function for the ground state. Note that it is obvious that the wave function is freely spread out along the wire.

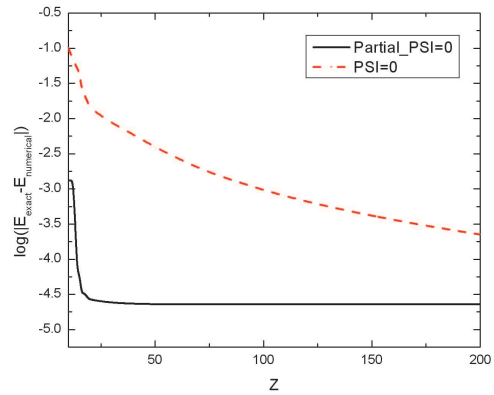

Fig. 2.2 Energy deviation plot (logarithmic scale) for $l = 0$ ground state, solid (dash) line for Neumann (Dirichlet) type boundary condition. $E_0 = \hbar^2/2mR^2$.

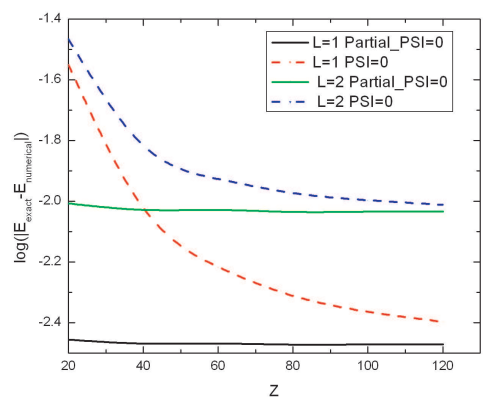

Fig. 2.3 Energy deviation plot (logarithmic scale) for $l = 1$ and $l = 2$ ground state. $E_0 = \hbar^2/2mR^2$.

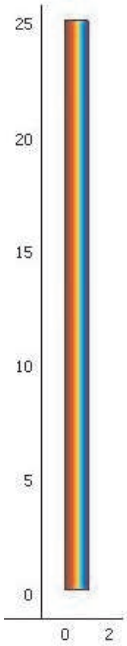

Fig. 2.4 Wave function plot for the ground state of the simple wire, top view.

3

Cylindrical nanowire with bulge

In this chapter, having established the basic model for a simple wire, we now proceed to the case of an irregularly shaped wire, i.e., a wire with a bulge. The introduction of a bulge to an ideal wire has multiple influence on the model: First, the wave function will become localized within the bulge area, resulting in a bound state; Second, the energy associated with each state will be reduced, giving rise to a binding energy.

3.1 A NUMERICAL STUDY OF A BULGED WIRE

The previous model was adapted to the model shown in Fig. 3.1, where H/R indicates the height of the bulge and W/R the width.
To study the effect of the bulge on the energy spectrum and wave function of the system, we used four sets of simulation conditions, namely, H/R varying from 0.1 to 1 while W/R=1, H/R varying from 0.1 to 1 while W/R=0.1, W/R varying from 0.1 to 1 while H/R=1, and W/R varying from 0.1 to 1 while H/R=0.1. The corresponding results are shown in Figs. 3.2-3.7.

As can be seen from the wave function plots and energy spectra, the bulge plays a major role in constructing the bound states which reduces the ground state energy of the ideal wire. For example, in Fig. 3.2, when H is relatively small, e.g., 0.1, the bulge is also small, therefore the wave function can spread along the z-axis direction, indicating relative freedom from bulge binding, and

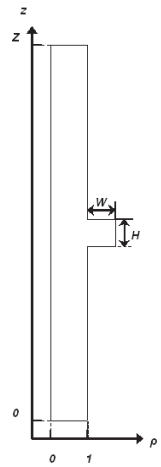

Fig. 3.1 The model for a bulged wire

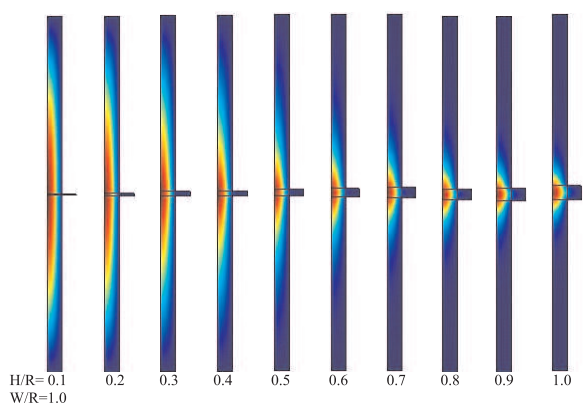

Fig. 3.2 Wave function plot for bulged wire with W/R=1, and H/R from 0.1 $\rightarrow$ 1

the corresponding ground state energy also approximates that of a bulgeless one. However, as H increases as well as the size of the bulge, the energetically preferential behavior for the wave function is no longer spreading, but concentrating within the bulge area, thereby giving rise to a bound state, of which the associated energy is shown in Fig. 3.4, where we can observe that the binding energy of the bound state increases with H (in other cases, with W), and that the magnitude of the increasing is also related to the size of the bulge, as can be seen from the sharper dropping behavior in the energy curve for $W = 1$ than for $W = 0.1$ in Fig. 3.4. More interestingly, of the two bulge parameters, the bulge height H is more significant, as first, in Fig. 3.6,

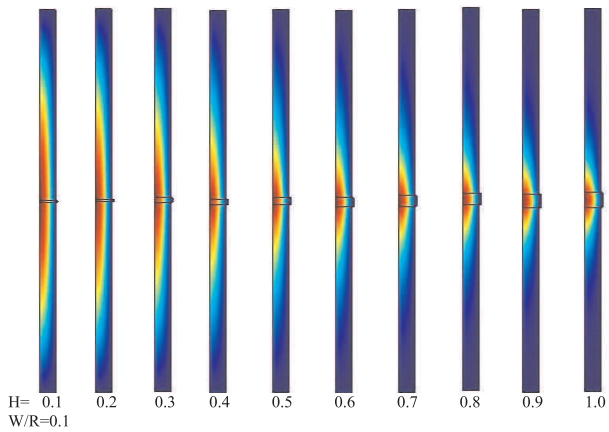

Fig. 3.3 Wave function plot for bulged wire with W/R=0.1, and H/R from 0.1 → 1

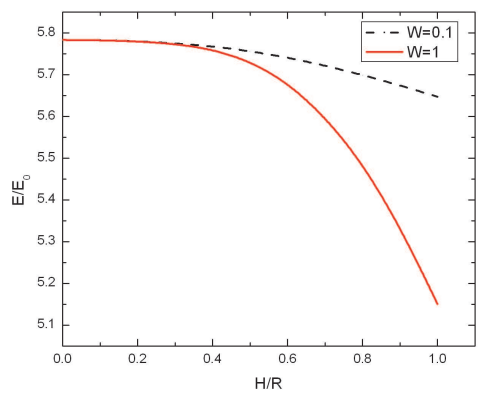

Fig. 3.4 Ground state energy spectrum for bulged wire with W/R=0.1 and 1.0 as indicated, and H/R from 0 → 1. E_0 is $\hbar^2/2mR^2$.

we observe that the wave functions all share the same spreading behavior, irregardless of the variation in W; and second, in Fig. 3.7, we also observe a similar invariance in the energy curve for $H = 0.1$. On the other hand, in case of $H = 1.0$, we observe that the wave function quickly adopts the concentrating behavior in Fig. 3.5, and that there is an even sharper dropping in the energy curve for $H = 1.0$ in Fig. 3.7. Therefore, we recognize the bulge height parameter H as largely determining the behavior of the energy spectrum curve.

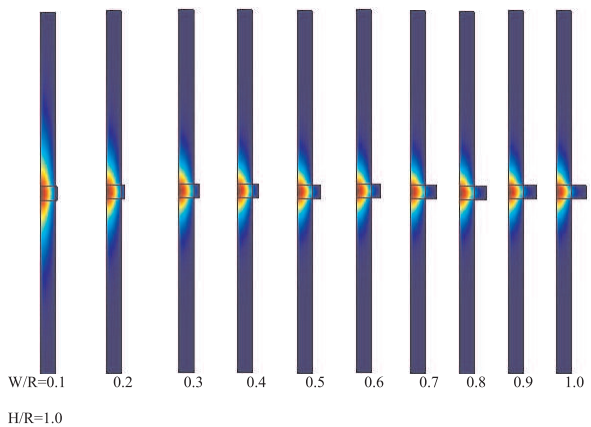

Fig. 3.5 Wave function plot for bulged wire with H/R=1, and W/R from 0.1 → 1

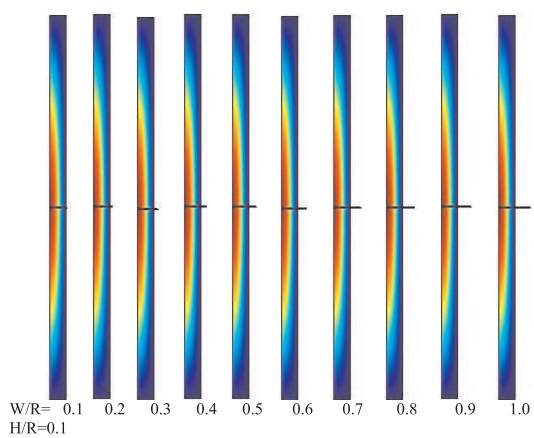

Fig. 3.6 Wave function plot for bulged wire with H/R=0.1, and W/R from 0.1 → 1

3.2 A DISCUSSION ON THE PARAMETER $\langle Z^2 \rangle$

One of the ways to characterize bound states in our wire is to calculate $\langle z^2 \rangle$, the average of z^2, namely, to determine how "spread-out" the wave function might be. The results are shown in Fig. 3.8.

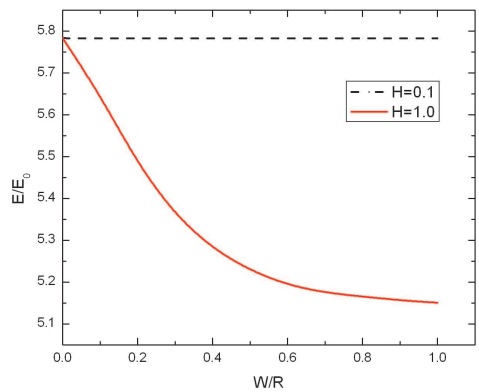

Fig. 3.7 Ground state energy spectrum for bulged wire with H/R=0.1 and 1.0 as indicated, and W/R from $0 \to 1$. E_0 is $\hbar^2/2mR^2$.

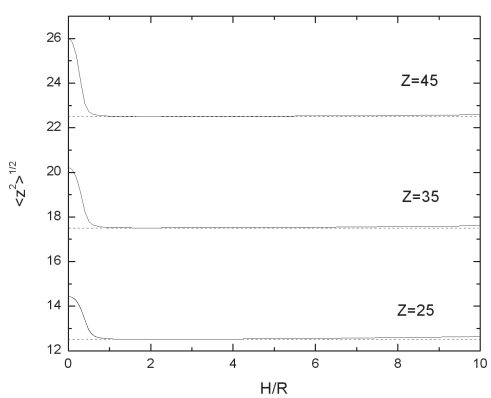

Fig. 3.8 Square root of average of z square for a wire of length $Z/R = 25, 35, 45$, respectively. Dashed lines indicate the minimum of the solid curves, note that there is a noticeable up-curving as H/R ($\gg 1$) increases

We expect the $\sqrt{\langle z^2 \rangle}$ curve to approach infinity when the parameter H/R goes to zero as the bulge becomes more and more insignificant or when the parameter H/R becomes comparable to the wire length as the wave function can now relatively "spread out" free of bounding. The actual "flat-out" behavior near $H/R = 0$ is due to the fact that we use wires with finite length, and from Fig. 3.9, it is clear that, if we take a longer length, the curve of

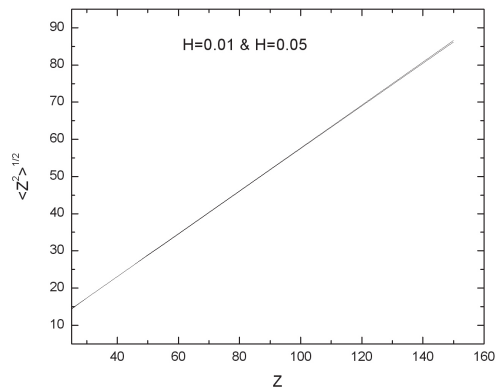

Fig. 3.9 $\sqrt{\langle z^2 \rangle}$ as function of wire length Z/R, with H/R set to 0.01 and 0.05, note that two lines for both heights almost overlap.

$\sqrt{\langle z^2 \rangle}$ tends to increase linearly, as can be understood as follows.
Note that since the bulge is small, we can assume, for the ground state, with Neumann and periodic boundary condition,

$$\begin{cases} \psi = const = C \\ \int \mid \psi(\rho, z) \mid^2 \rho dz d\rho = 1 \end{cases}$$

therefore

$$\frac{1}{2} C^2 (Z/R) = 1, \tag{3.1}$$

where Z/R is the length of the wire, which gives $C = \sqrt{2}/\sqrt{Z/R}$, and therefore

$$\sqrt{\langle z^2 \rangle} = \sqrt{\iint \mid \psi(\rho, z) \mid^2 z^2 \rho d\rho dz} = Z/\sqrt{3}R \tag{3.2}$$

which clearly establishes that, for a very small bulge, $\sqrt{\langle z^2 \rangle}$ is linearly dependent on the wire length Z/R, in other words, it means, when the bulge is sufficiently small, the wire length Z/R is by large the main parameter that determines the behavior of the wave function, and if Z/R goes to infinity, as in an ideal wire, the wave function will also spread to infinity, just as in an ideal wire.
After we have discussed the ground state results, we now move on to the excited state, the study of which would reveal useful information for the bound states. We first present here the evolution of an excited state, and then a thorough picture of the first excited state is produced, finally a brief coverage of higher excited levels (up to 10) is given.

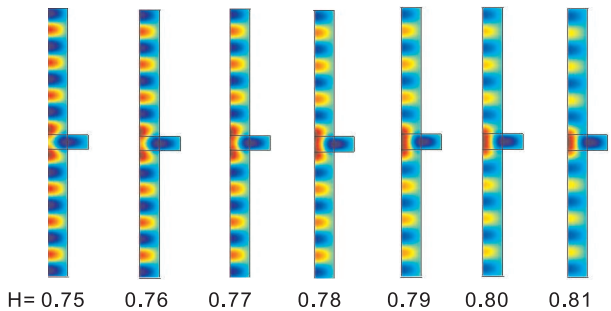

Fig. 3.10 Evolution of an excited state according to variation in H/R, W/R is 1.0. Contour plot of the wave function is shown.

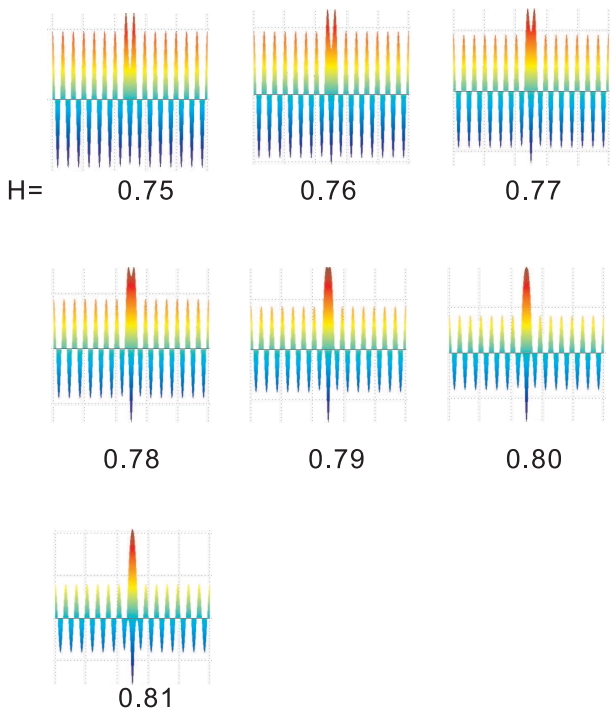

Fig. 3.11 Evolution of an excited state according to variation in H/R, W/R is 1.0. side view of the wave function.

As shown in Fig. 3.10 and Fig. 3.11, a typical bound state within a bulged wire configuration evolves according to the variation of the bulge parameter, i.e., as the bulge height increases, two adjacent peaks in the wave function would move closer until they merge into one while pushing the valley between them into the bulge area, forming so-called excited state.

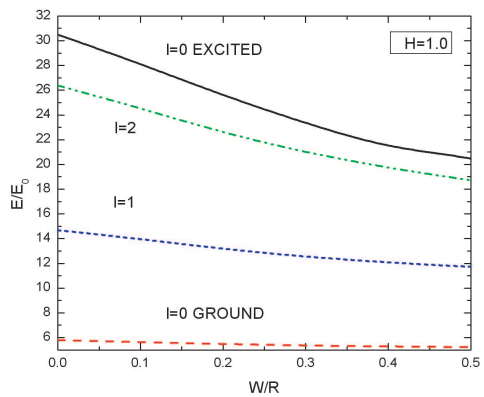

Fig. 3.12 Energy spectrum for ground states of l=0, l=1 and l=2 and excited state of l=0, with variation in W/R from $0 \rightarrow 0.5$, and H/R 1. E_0 is $\hbar^2/2mR^2$.

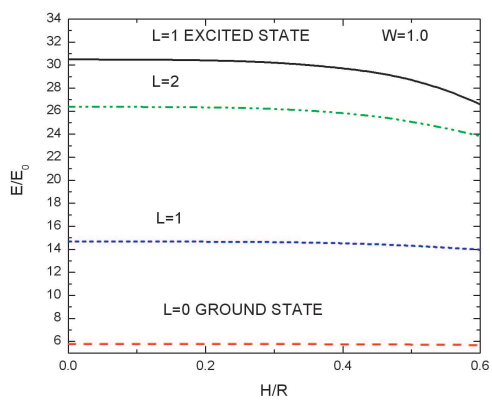

Fig. 3.13 Energy spectrum for ground states of l=0, l=1 and l=2 and excited state of l=0, with variation in H/R from $0 \rightarrow 0.5$, and W/R 1. E_0 is $\hbar^2/2mR^2$.

One of the most noticeable features of the excited state is the extra peaks along the $z-$axis. We attribute this feature to the fact that we used wires of finite length instead of infinite ones, therefore giving rise to the resonant state where particles can "oscillate" relatively freely along the wire. Nevertheless, this "finite wire length effect" will decrease as the wire length Z/R increases towards infinity.

Tracing these states, we then can trace the energy spectrum of the first

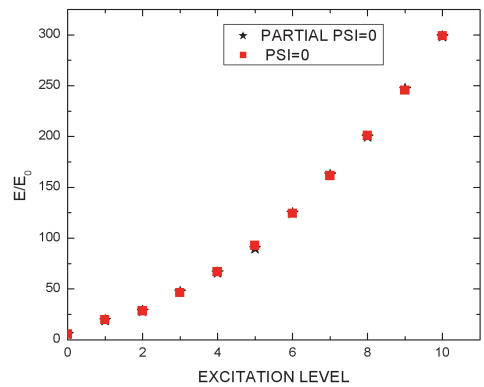

Fig. 3.14 Energy of higher excited states for l=0. Stars (squares) indicate Neumann (Dirichlet) boundary condition.

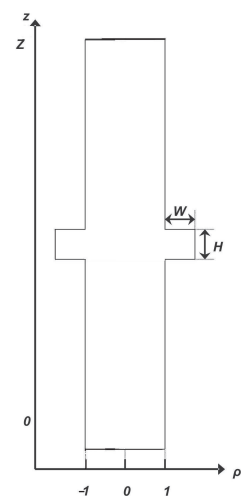

Fig. 3.15 The model for a 2D bulged wire.

four lowest levels, including ground states of l=0, 1, and 2 and excited state of l=0 as a function of varying bulge parameters, as shown in Fig. 3.12 and Fig. 3.13.

Finally, we present a brief example of higher excited levels, here for H/R=0.8, W/R=1.0, and excited levels up to 10, for both types of boundary conditions used, as shown in Fig. 3.14.

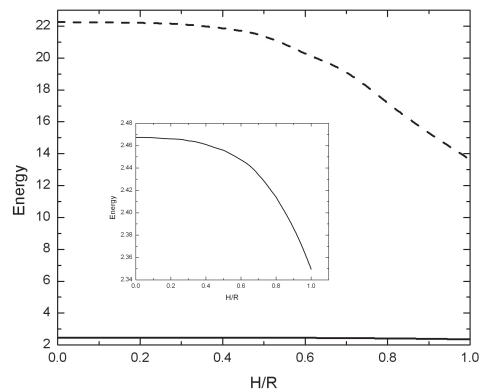

Fig. 3.16 Energy spectra for a 2D wire with bulge of bulge width W/R 1.0 and bulge height H/R from 0.1 to 1.0 , solid line indicates ground state, and dash line first excited state. Inset is the energy spectrum for ground state only.

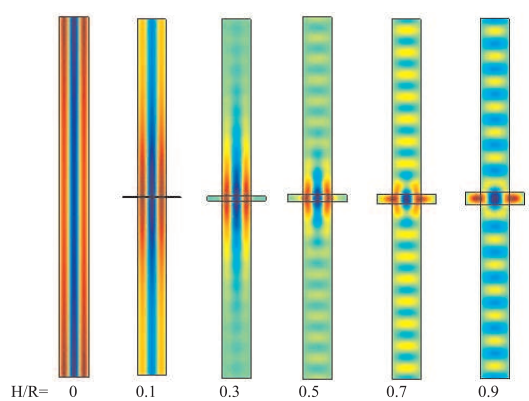

Fig. 3.17 Wave function plots for bulge wire of bulge width W/R=1 and bulge height H/R 0, 0.1, 0.3, 0.5, 0.7 and 0.9, respectively.

3.3 A COMPARISON WITH A 2D MODEL

We now introduce a 2D wire model as a brief comparison to our 3D model. In this 2D rectangular coordinates, Eq. (2.1) becomes

$$\frac{\partial^2\varphi}{\partial\rho'^2} + \frac{\partial^2\varphi}{\partial z'^2} + \epsilon\varphi = 0 \tag{3.3}$$

and then we proceed as in the case of our 3D wire, using a wire of length 25 and Neumann and periodic boundary condition to find the ground state

and first excited state for different bulged wire configuration. The result for a bulged wire of bulge width W/R=l 1.0 and bulge height H/R from 0.1 to 1.0 is shown as the energy spectra in Fig. 3.16 and wave function plots in Fig. 3.17. As can be seen from Fig. 3.16, the energy curve behaves exactly the same as the 3D wire case in Fig. 3.2 for the same bulge setting, and a similarity to how the wave function for the excited state gradually become localized in the bulge with increasing bulge size as expected.

4

Cylindrical wire with magnetic field

In this chapter, we will study the effect of a magnetic field on the cylindrical wire with and without bulge. First, we will solve analytically and numerically the problem of an infinitely long cylindrical wire in a magnetic field directed along the wire axis, later we will compare these results to the numerically obtained results for a wire with bulge in a magnetic field.

4.1 ANALYTICAL CALCULATIONS FOR THE INFINITELY LONG CYLINDRICAL WIRE

We consider a circular wire with radius R. We will now try to find the eigenvalues and eigenvectors of the following Schrödinger equation

$$\frac{1}{2m}\left(-i\hbar\vec{\nabla}+\frac{e}{c}\vec{A}\right)^2\psi+V\psi=E\psi \tag{4.1}$$

where $\vec{A}$ represents the vector potential and V the confinement potential as defined in Eq. (2.1). For the sake of simplicity, we will omit the z-dependence in any further calculations.

Due to the symmetry of the problem, we may benefit from the symmetric gauge $\vec{A}=\frac{1}{2}B\rho\vec{e}_\theta$. Introducing the cyclotron frequency $\omega_c=eB/mc$, we can

rewrite the Hamiltonian into

$$\begin{aligned} H &= \frac{1}{2m}\left(-i\hbar\vec{\nabla}+\frac{e}{c}\vec{A}\right)^2 \\ &= -\frac{\hbar^2}{2m}\frac{1}{\rho}\frac{\partial}{\partial\rho}\rho\frac{\partial}{\partial\rho}-\frac{\hbar^2}{2m}\frac{1}{\rho^2}\frac{\partial^2}{\partial\theta^2}-i\frac{\hbar\omega_c}{2}\frac{\partial}{\partial\theta}+\frac{m\omega_c^2}{8}\rho^2. \end{aligned} \tag{4.2}$$

Since $[H, L_z] = 0$, where L_z is the angular momentum operator along the z-axis, we know that $\langle L_z\rangle$ is a conserved quantity and therefore we may write $\psi(\rho,\theta) = \varrho(\rho)e^{il\theta}$. The Schrödinger equation can then be rewritten, so the only unknown part of the wave function is then the part that describes the radial dependence of the solution.

$$\left(\frac{\partial^2}{\partial\rho^2}+\frac{1}{\rho}\frac{\partial}{\partial\rho}-\frac{l^2}{\rho^2}\right)\varrho+\left(\frac{m\omega_c}{\hbar}l-\left(\frac{m\omega_c}{2\hbar}\right)^2\rho^2+\frac{2mE}{\hbar^2}\right)\varrho=0. \tag{4.3}$$

Introducing

$$k^{*^2} = l\frac{m\omega_c}{\hbar}+\frac{2mE}{\hbar^2}, \tag{4.4a}$$

$$\lambda = \frac{m\omega_c}{2\hbar}, \tag{4.4b}$$

we find that

$$\left(\varrho''+\frac{1}{\rho}\varrho'-\frac{l^2}{\rho^2}\varrho\right)+\left(k^{*^2}-\lambda^2\rho^2\right)\varrho=0. \tag{4.5}$$

It is instructive now to study the above mentioned equation for large and small values of ρ in order to construct an appropriate solution for the function $\varrho(\rho)$. For $\rho\to\infty$ we find that

$$\varrho''-\lambda^2\rho^2\varrho=0 \qquad\longrightarrow\qquad \varrho(\rho)\propto e^{-\frac{\lambda}{2}\rho^2}, \tag{4.6}$$

whereas for $\rho\to 0$ the equation reads

$$\varrho'-\frac{l^2}{\rho}\varrho=0 \qquad\longrightarrow\qquad \varrho(\rho)\propto\rho^{|l|}. \tag{4.7}$$

From this analysis we can conclude that $\varrho(\rho)=\rho^{|l|}e^{-\frac{\lambda}{2}\rho^2}f(\rho)$. Substituting this expression into Eq. (4.5) results in

$$f''+f'\left(\frac{2\,|l|+1}{\rho}-2\lambda\rho\right)-\left(2\lambda(|l|+1)-k^{*^2}\right)f=0, \tag{4.8}$$

where f' stands for $\frac{\partial f}{\partial\rho}$. Finally, we introduce the following substitution

$$t=\lambda\rho^2, \tag{4.9}$$

which enables us to rewrite Eq. 4.8 to

$$tf'' + ((|l|+1) - t)f' - \left(\frac{1}{2}(|l|+1) - \frac{k^{*^2}}{4\lambda}\right) f = 0, \tag{4.10}$$

where f' now stands for $\frac{\partial f}{\partial t}$. This differential equation can be solved analytically and the solutions are known as the confluent hypergeometric functions [13][14]

$$f(t) = {}_1F_1(-n_r; |l|+1; t) \qquad \text{and} \qquad -n_r = \frac{1}{2}(|l|+1) - \frac{k^{*^2}}{4\lambda}. \tag{4.11}$$

The boundary conditions impose that the wave function must be zero at the border of the circular well, thus

$${}_1F_1(-n_r; |l|+1; \lambda R^2) = 0 \tag{4.12}$$

from which the parameter n_r can be found. The final result for the wave function can thus be written as

$$\psi_{nl} = C_{n_r l} e^{il\theta} \rho^{|l|} e^{-\frac{\lambda}{2}\rho^2} \; {}_1F_1(-n_r; |l|+1; \lambda\rho^2). \tag{4.13}$$

with $C_{n_r l}$ a normalization constant. From Eq. (4.4) and Eq. (4.11) we find that

$$-n_r = \frac{1}{2}(|l|+1) - l\frac{m\omega_c}{4\lambda\hbar} + \frac{2mE}{4\lambda\hbar^2}, \tag{4.14}$$

so we can write

$$E_{nl} = \hbar\omega_c \left(n_r + \frac{1+|l|-l}{2}\right). \tag{4.15}$$

4.2 NUMERICAL CALCULATIONS FOR THE INFINITELY LONG CYLINDRICAL WIRE

In order to solve Eq. (4.1) numerically, we will again make use of COMSOL. Let

$$\Phi = BS = B\pi R^2 \tag{4.16a}$$

$$\Phi_0 = \frac{hc}{e} \tag{4.16b}$$

and introducing R and $\frac{\hbar^2}{2m\pi R^2}$ as units of length and energy to obtain a dimensionless Schrödinger equation, we find

$$\frac{\partial^2 \varrho}{\partial \rho^2} + \frac{1}{\rho}\frac{\partial \varrho}{\partial \rho} - \frac{l^2}{\rho^2}\varrho + \left(\frac{E}{\pi} + 2l \cdot \frac{\Phi}{\Phi_0} - \frac{1}{\rho^2}\frac{\Phi^2}{\Phi_0^2}\right)\varrho = 0 \tag{4.17}$$

where ρ and E are now in dimensionless units. The calculated energy spectrum is given in Fig. 4.1, and matches the analytical result.

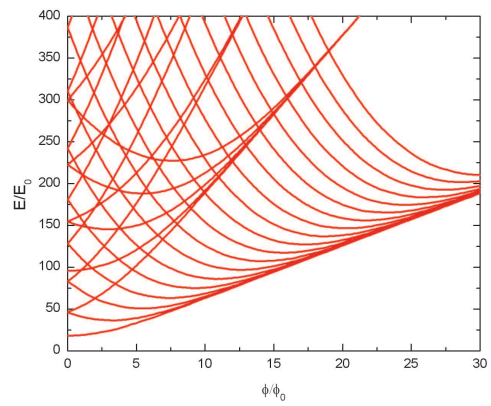

Fig. 4.1 The energy spectrum of an infinite wire in a magnetic field

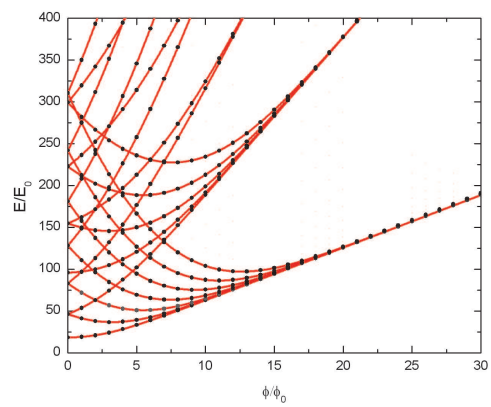

Fig. 4.2 Part of the energy spectrum of a finite wire in a magnetic field, indicated by symbols, against infinite wire indicated by lines, for l up to ± 6.

4.3 NUMERICAL SOLUTION FOR A FINITE CYLINDRICAL WIRE

In order to investigate the energy as a function of local thickness variations, we need to insert $\psi = \varrho(\rho, z)e^{il\theta}$ in Eq. (4.1), which results in

$$\frac{\partial^2 \varrho}{\partial \rho^2} + \frac{1}{\rho}\frac{\partial \varrho}{\partial \rho} + \frac{\partial^2 \varrho}{\partial z^2} - \frac{L^2}{\rho^2}\varrho + \left(\frac{E}{\pi} + 2l \cdot \frac{\Phi}{\Phi_0} - \frac{1}{\rho^2}\frac{\Phi^2}{\Phi_0^2 \rho^2}\right)\varrho = 0 \qquad (4.18)$$

By doing this, we introduce an error again compared to the infinite wire, since

we take the wire to have a finite length. The energy spectrum can again be seen in Fig. 4.2 where it is plotted together with the spectrum of an infinite wire. We use for the simulation the same condition as before in the cylindrical wire case, i.e., the wire length Z is 25, Neumann and periodic boundary conditions are used. It is clear that there is no noticeable difference between both spectra, indicating that the induced error is small, similar to the case of the cylindrical wire. However, we would like to add that the magnetic field, despite its relatively small influence when weak, will serve to spread the wave function along the $z-$axis while squeezing it towards the radial axis, which will be discussed later on, and this spreading effect with respect to the strength of magnetic field would diminish the accuracy of our assumption about the sufficient wire length for the simulation. Nevertheless, we checked that the error induced by this effect is still small enough within our magnetic field's strength range. Furthermore, it is worth mentioning that, in both cases of infinite and finite wire, the magnetic influence shows strong predominance, compared to the wire wall binding, when the magnetic field is relatively strong, up to 20 (see Fig. 4.2 where different ground state energy spectra for, e.g., different positive l already converge into one line for ϕ/ϕ_0=20), leading to the so-called Landau levels.

4.4 NUMERICAL SOLUTION FOR A BULGED WIRE

We now proceed to investigate the effect of a magnetic field applied along the $z-$axis on a bulged wire. The bulged wire itself is the same model as in Fig. 3.1. The simulation runs with variation in three parameters, bulge height H/R, bulge width W/R and magnetic field strength ϕ/ϕ_0, with H/R= 0.5 and 1, W/R=0.5 and 1 and ϕ/ϕ_0 from $0 \rightarrow 30$, respectively. The results are shown in Figs. 4.3-4.6.

As seen from Figs. 4.3-4.6, the bulge exerts its influence in the energy spectrum by creating the energy shift from the bulgeless wire, and the magnitude of the shift is related to the bulge parameter, H and W, as similar to the case of bulged wire. Nevertheless, as the magnetic field grows stronger, the shift decreases, indicating the presence of magnetic confinement, instead of the actual wire-wall confinement. We can clarify this further with the concept of "magnetic length", i.e., the natural length scale of a wave function in a magnetic field, as defined by

$$l_0 = \sqrt{\frac{hc}{eB}} = \sqrt{\frac{\phi_0}{\phi} \cdot \pi R^2} \tag{4.19}$$

Therefore, the ratio of l_0 to R is a characteristic parameter in determining the behavior of the wave function, especially along the radial direction. From Eq. (4.4), it is clear that the magnetic length is comparable to the wire radius

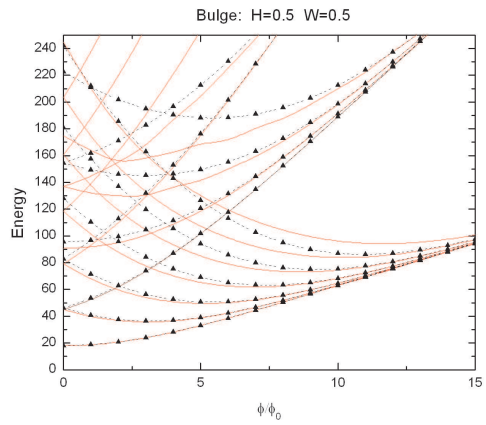

Fig. 4.3 Part of the energy spectrum of a finite bulged wire under magnetic field, with W=0.5 and H=0.5,indicated by lines, against infinite wire indicated by symbols and dashes.

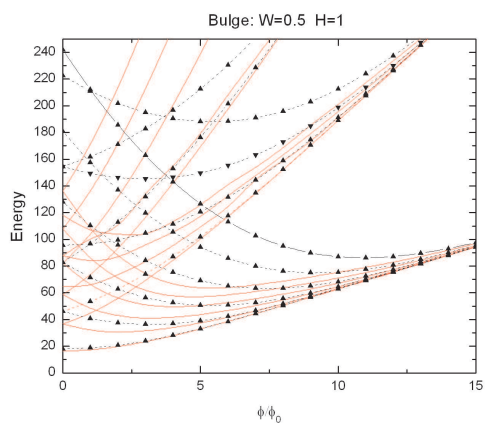

Fig. 4.4 Part of the energy spectrum of a finite bulged wire under magnetic field,with W=0.5 and H=1, indicated by lines, against infinite wire indicated by symbols and dashes.

when $\frac{\phi}{\phi_0} = \pi$, or bigger. Therefore we trace the behavior of wave function of ground state around this value, and the result is shown in Figs. 4.7 and 4.8.

It can be seen from Figs. 4.7 and 4.8 that, as the magnetic field strength increases, the wave function clearly gets more and more concentrated towards the $z-$axis while freeing itself from the bulge binding and spreading along the length, up to ϕ/ϕ_0=8, the wave function already resembles very much that of

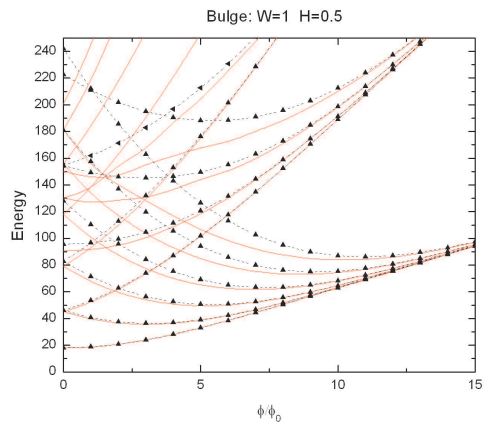

Fig. 4.5 Part of the energy spectrum of a finite bulged wire under magnetic field,with W=1 and H=0.5, indicated by lines, against infinite wire indicated by symbols and dashes.

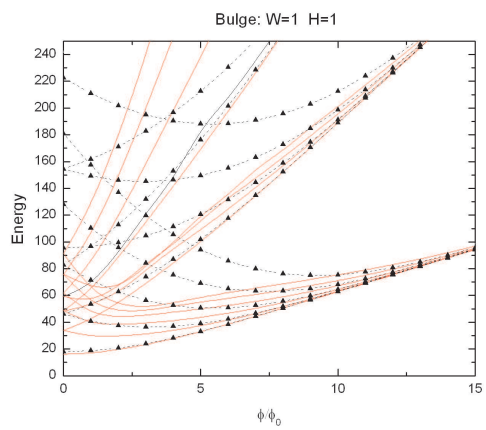

Fig. 4.6 Part of the energy spectrum of a finite bulged wire under magnetic field,with W=1 and H=1, indicated by lines, against infinite wire indicated by symbols and dashes.

a bulgeless wire, nevertheless, it is Landau level predominated by magnetic field instead of wire wall binding.

As for the influence of magnetic field on the excited states, such as the ones in Fig. 4.9, we observe that in the near-edge region of the wave function there is small oscillation, which is gradually reduced by the strengthening magnetic field, therefore we trace the variation of maximal oscillation amplitude of the

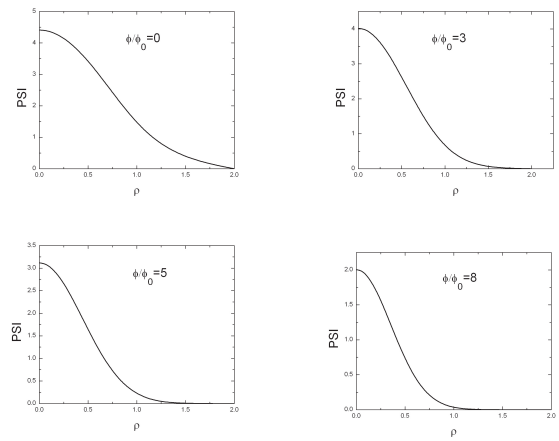

Fig. 4.7 The wave function as a function of ρ, at $z = 12.5$, for ϕ/ϕ_0=0, 3, 5 and 8, respectively, for $l = 0$ ground state.

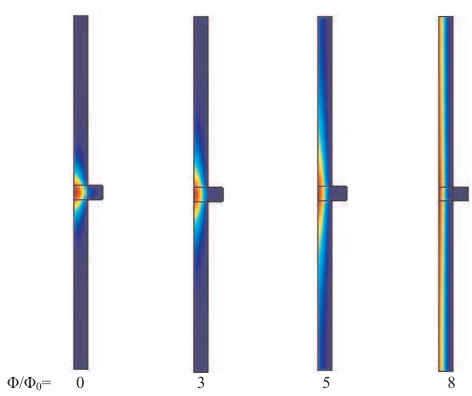

Fig. 4.8 The top views of wave function plots for ϕ/ϕ_0=0, 3, 5 and 8, respectively, for $l = 0$, ground state.

normalized wave function ψ in the near-edge region, i.e., $\psi_{MAX}\mid_{edge}$, according to the variation of the magnetic field. The result is shown in Fig. 4.10, from which, we observe that the magnetic field clearly reduces the minor oscillation along the wire length, giving rise to a critical field strength at which minimal minor oscillation is achieved, 9 for $l = 0$ and 11 for $l = 1$, and that after the critical point where the wave function is largely "smoothed", the $\psi_{MAX}\mid_{edge}$ starts to increase, which, however, we attribute to the same spreading effect of magnetic field as before in the ground state case. The binding energy of aforementioned excited states also corresponds to this critical phenomenon,

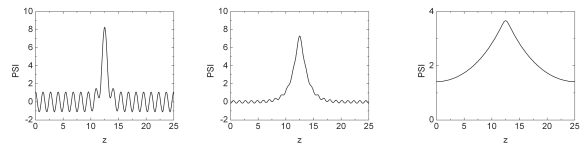

Fig. 4.9 The wave function plots on the cross-section at $\rho = 0$ for ϕ/ϕ_0=4, 8 and 12, respectively.

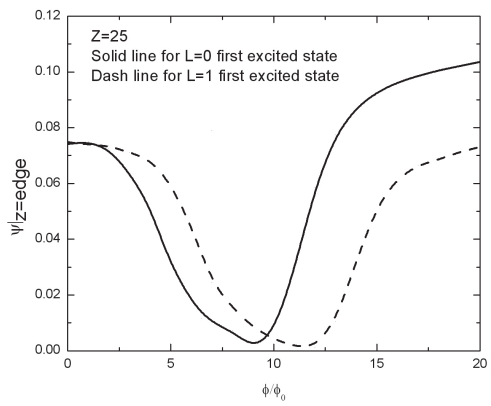

Fig. 4.10 Maximal oscillation amplitude of the normalized wave function ψ in the near-edge region as a function of magnetic field strength, ϕ/ϕ_0. Solid line indicates $l = 0$ first excited state, and dash line $l = 1$ first excited state.

as the energy reaches minimum at ϕ/ϕ_0=9 for $l = 0$ and ϕ/ϕ_0=11 for $l = 1$, as seen in Fig. 4.11.

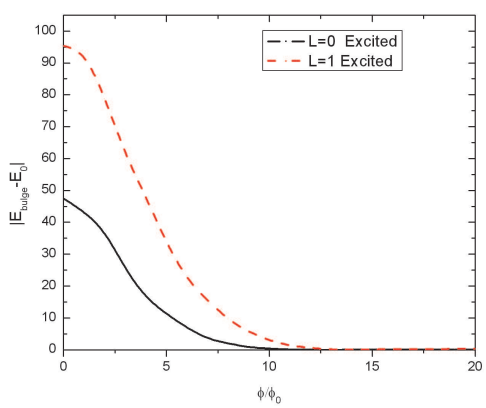

Fig. 4.11 The binding energy for the bound excited state of a bulged wire in a magnetic field, solid line indicates $l = 0$ first excited state, and dash line $l = 1$ first excited state. E_0 is the corresponding energy for a bulgeless wire.

5

Conclusion

In this thesis we studied extensively some of the important aspects of nanowires regarding its energy spectrum and electronic wave function behavior in a specific structural configuration as well as under certain external influence.
This thesis started with a short introduction to some important properties of nanowires and the methods used to grow it.
To fulfill our goal of a numerical study of nanowires, we established a model adaptable to various structural configurations and/or external potentials for solving the cylindrical Schrödinger equation using a finite difference approach.
From our calculations, by comparing results for the finite wire and the infinite wire, we first determined a suitable aspect ratio parameter as well as the proper boundary conditions for a sound basis for further simulations.
A study of the localization effect of an extra bulge on a cylindrical wire is then given in detail. We found that the bulge size parameters largely determine the localization of the wave function, namely, the bound state, the binding energy associated to them, and how both of them vary according to the variation of the parameters.
We then studied the effect of magnetic field on the nanowire. With the addition of the magnetic parameter, we are able to trace the response of the bound state and the binding energy to the external (magnetic) potential. It is worth mentioning that, in the end of this thesis, by means of the magnetic length and the maximal near-edge oscillation we determine the critical points for magnetic effect dominance for both ground state and excited state.

References

1. Ji, Chunhai. Guliants, Elena A. Abeysinghe, Don. Anderson, Wayne A. *Materials Research Society Symposium - Proceedings*, Vol. **728** 157 (2002)

2. MH Huang, *et al.*, *Science*, Vol. **292**, No. (5523), 1897 (2001)

3. Lieber, C.M., *et al*, in *Proceedings of the Robert A. Welch Foundation 40th Conference on chemical Research: Chemistry on the Nanometer Scale*, p.165. R.A. Welch Foundation, Houston, 1997

4. Wagner, R.S., in *A.P. Levitt(Ed), Whisker Technology*, Wiley, New York, 1970, 47-119

5. Givargizov, E.I., in *Growth of Crystals* , Kluwer Academic Pub, 2002

6. Hiruma, H., *et al*, *J.Appl.Phys.* **77**, 447 (1995)

7. Cui, Y., Lieber, C.L., *Science*, **291**, 851 (2001)

8. Wang, J., *et al*,*Science*, **293**, 1455 (2001)

9. Cui, Y., *et al*, *Science*,**293**, 1289 (2001)

10. Lieber, C.M., *Solid State Communications*, Vol. **107**, No. 11, 607 (1998)

11. Samuelson, L., *et al*, *Physica E*, **21**, 560 (2004)

12. Voit, J., *Phys. Rev. B*, **47**, 6740, (1993)

13. Flügge, S., *Practical Quantum Mechanics*, Springer-Verlag, New York, 1974)

14. Abramowitz, M. and Stegun, I., *Handbook of mathematical functions*, Dover, New York, 1970